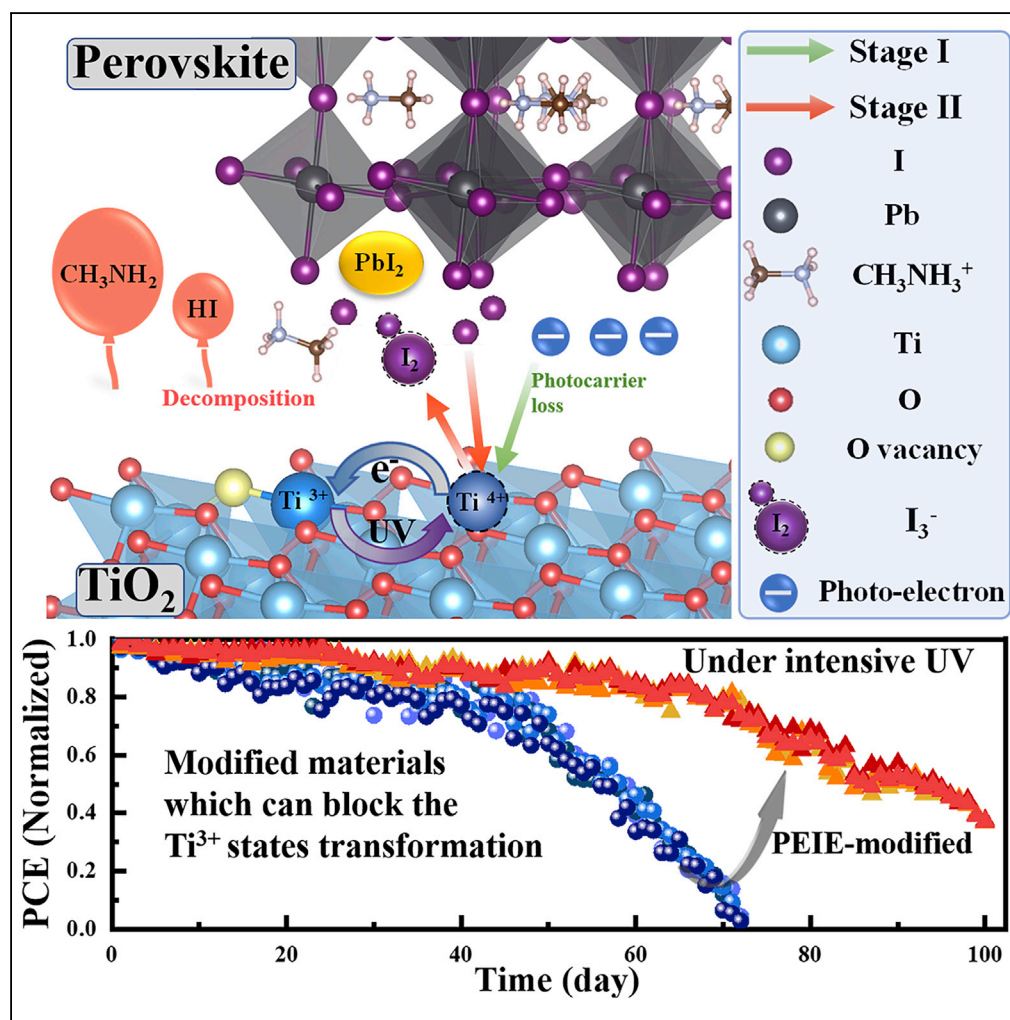Article

Two-Stage Ultraviolet Degradation of Perovskite Solar Cells Induced by the Oxygen Vacancy-Ti^{4+} States

Jun Ji, Xin Liu, Haoran Jiang, ..., Dong Wei, Yingfeng Li, Meicheng Li

mcli@ncepu.edu.cn

HIGHLIGHTS

A two-stage degradation process of TiO$_2$-based PSCs under continuous UV irradiation

The transformation of Ti^{3+}-V$_O$ to Ti^{4+}-V$_O$ states is responsible for the UV degradation

A universal method to enhance the UV stability of PSCs was proposed

Article

Two-Stage Ultraviolet Degradation of Perovskite Solar Cells Induced by the Oxygen Vacancy-Ti^{4+} States

Jun Ji,[1,2] Xin Liu,[1,2] Haoran Jiang,[1] Mingjun Duan,[1] Benyu Liu,[1] Hao Huang,[1] Dong Wei,[1] Yingfeng Li,[1] and Meicheng Li[1,3,*]

SUMMARY

The failure of perovskite solar cells (PSCs) under ultraviolet (UV) irradiation is a serious barrier of commercial utilization. Here, a two-stage degradation process of TiO$_2$-based PSCs is discovered under continuous UV irradiation in an inert atmosphere. In the first decay stage, oxygen vacancy-Ti^{3+} (Ti^{3+}-V$_O$) transform into active Ti^{4+}-V$_O$ trap states under UV excitation and cause photocarrier loss. Furthermore, Ti^{4+}-V$_O$ states can convert back into Ti^{3+}-V$_O$ states through oxidizing I$^-$, which result in the accumulation of I$_3^-$. Sequentially, the rapid decomposition of perovskite accelerated by increasing I$_3^-$ replaces the photocarrier loss as the dominant mechanism leading to the second decay stage. Then, a universal method is proposed to improve the UV stability by blocking the transformation of Ti^{3+}-V$_O$ states, which can be realized by polyethyleneimine ethoxylated (PEIE) modified layer. The optimized devices remain ∼75% of its initial efficiency (20.51%) under UV irradiation at 72 days, whereas the normal devices fail completely.

INTRODUCTION

Organic-inorganic lead halide perovskite solar cells (PSCs) show great potential to become the promising candidate for future energy conversion device (Tsai et al., 2018; Jeon et al., 2015; Yang et al., 2019; Bai et al., 2019; Cui et al., 2019), with the latest certification efficiency of 25.2% (Best, 2019). The most popular electron transport layer (ETL) in the high-performance PSCs is the inorganic compact TiO$_2$ owing to its suitable band alignment and high transmittance (Kim et al., 2016; Niu et al., 2015). But the poor stability of TiO$_2$-based PSCs under working conditions still restricts its commercialization. Especially, the intrinsic instability of TiO$_2$-based PSCs under ultraviolet (UV) irradiation has attracted extensive attention.

To overcome UV instability of TiO$_2$-based PSCs, Al$_2$O$_3$, MgO, Sb$_2$S$_3$, etc. were used to suppress the continuous degradation by modifying, separating, or replacing TiO$_2$ ETL, which remained 70%–90% of the initial efficiency after hundreds of hours of UV exposure (Ito et al., 2014; Wei et al., 2016, 2019a; Han et al., 2015; Lee et al., 2018, 2019b; Wan et al., 2018). Meanwhile, the study of degradation mechanism is necessary to further improve the UV stability of PSCs. It is well known that the TiO$_2$ is photocatalytic, which can supply electrons to accelerate organic decomposition reactions. It can help to explain the decomposition of perovskite material under UV illumination with moisture or oxygen, which is responsible for the instability of PSCs (Ito et al., 2014; Aristidou et al., 2015; Abdelmageed et al., 2016; Shlenskaya et al., 2018). In terms of carrier transfer, the recombination loss induced by UV irradiation can also lead to the decay of PSCs performance with the assistance of oxygen vacancies in TiO$_2$ and oxygen molecules in air (Leijtens et al., 2013; Bryant et al., 2016). In addition, at the interface between TiO$_2$ and perovskite layers, the voltage loss due to the charge accumulation under light soaking can also cause the performance decrease of PSCs (Gottesman et al., 2016). However, the UV degradation of TiO$_2$-based PSCs performance still exists in the absence of moisture, oxygen, and visible light (Shin et al., 2017; Wang et al., 2019; Ahn et al., 2016), which is future work condition of PSCs. Therefore, the exploration of the UV-degradation process and the underlying mechanism of TiO$_2$-based PSCs in inert atmosphere become an important and practical research topic.

Here, long-term monitoring of PSCs performance under continuous UV irradiation in glovebox was conducted. We discovered the two-stage UV degradation of TiO$_2$-based PSCs and explored the underlying mechanism. Then, we proposed a universal method to inhibit the UV degradation of PSCs. And, polyethyleneimine ethoxylated (PEIE)-modified layer was introduced on TiO$_2$ ETL, obtaining UV stable PSCs with

[1]State Key Laboratory of Alternate Electrical Power System with Renewable Energy Sources, School of Renewable Energy, North China Electric Power University, Beijing 102206, China
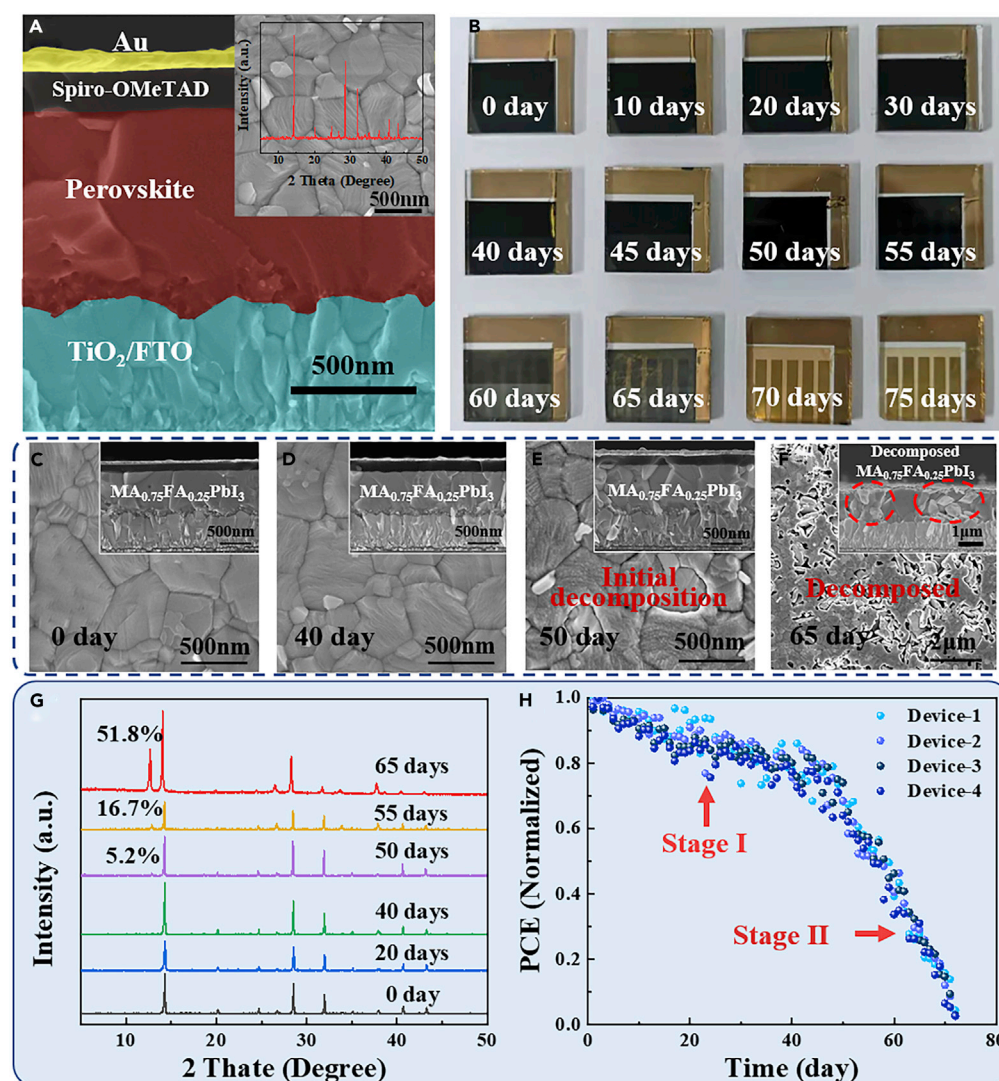
[2]These authors contributed equally

[3]Lead Contact

*Correspondence: mcli@ncepu.edu.cn

https://doi.org/10.1016/j.isci.2020.101013

Figure 1. Degradation of the Perovskite Solar Cells under UV Irradiation

(A) SEM cross-sectional image of PSCs. The layers from the bottom up are: FTO, TiO_2, $MA_{0.75}FA_{0.25}PbI_3$, spiro-OMeTAD (doped with Li-TFSI, FK 209, and TBP), and Au. And the inserted images are top-view SEM image and XRD patterns of the corresponding perovskite film.

(B) The photographs of PSCs for different UV exposure time.

(C–F) The SEM images of the $MA_{0.75}FA_{0.25}PbI_3$ films had been prepared in solar cells after UV irradiation for 0, 40, 50, and 65 days.

(G) XRD patterns for $MA_{0.75}FA_{0.25}PbI_3$ in PSCs under UV irradiation for different times.

(H) The evolution of the normalized PCE of the PSCs under UV irradiation for 72 days. For the perovskite film measurements, the Au electrodes were removed with tapes and the Spiro-based HTL were rinsed with chlorobenzene.

high champion efficiency of up to 20.51%, which held ~75% of the initial efficiency when the normal PSCs failed completely after ~72 days intensive UV irradiation. This method provides a promising way to develop UV-stable and high-performance perovskite solar cells.

RESULTS AND DISCUSSION

The Two-Stage Degradation under UV Irradiation

In this work, we prepared planar perovskite solar cells (PSCs) structured as glass/FTO/c-TiO_2/perovskite/ spiro-OMeTAD/Au using the convenient one-step solution method. The detailed fabrication procedures are shown in the Transparent Methods section of Supplemental Information. Figure 1A shows the cross-

sectional scanning electron microscopy (SEM) image of the PSCs, wherein $MA_{0.75}FA_{0.25}PbI_3$ was used as the perovskite absorber material. Meanwhile, the compact TiO_2 and the 2,2′,7,7′-tetrakis (N, N-di-p-methoxy-phenylamine)-9,9′ spirobifluorene (spiro-OMeTAD) serve as the electron transport layer (ETL) and hole transport layer (HTL), respectively. As seen, the thickness of the perovskite layer is ∼700 nm. The top-view SEM image and XRD pattern inserted in Figure 1A indicate the uniform and high-quality perovskite film, which is similar to our previous reports (Song et al., 2016; Cui et al., 2017; Wei et al., 2019a, 2019b).

In order to explore the influence of UV irradiation on PSCs, we first observed the deterioration of perovskite films in PSCs after continuous UV exposure. Here, we used Philip UV lamp (λ = 254 nm) with an intensity of ∼50 mW·cm^{-2} (equivalent to 11 suns of UV light below 400 nm) to irradiate the PSCs from the TiO_2 ETL side at room temperature in an argon-filled glovebox. All UV irradiation treatments of PSCs for this work were carried out under such UV radiation conditions, unless otherwise specified. This is a rather brutal test that helps to quickly identify the degradation rule of PSCs under UV irradiation. Figure 1B shows the photographs of PSCs for different UV exposure times. We found that perovskite films prepared on TiO_2 remained uniform black phase for ∼50 days, until dramatic yellow phase transition began around 55 days. In general, the black phase of the absorber material is recognized as perovskite structure and the yellow phase can be recognized as PbI_2. Hence, it is speculated that the decomposition of perovskite film could occur rapidly after a lag time of ∼50 days under such a UV irradiation condition. Furthermore, the top-view SEM images of perovskite film in UV-irradiated PSCs are shown in Figures 1C–1F, which reflect the evolution of perovskite film morphologies. Apparently, the film morphology did not change significantly at the early stage (within 50 days). After this time threshold, the perovskite films began to collapse and a new cleavage surface appeared, indicating the initial decomposition. On the 65th day, a large number of holes appeared in the perovskite films, demonstrating the serious decomposition and deterioration of the perovskite film. In addition, the perovskite film without underlying TiO_2 ETL shows excellent stability under the same UV irradiation condition and did not decompose significantly within 150 days, as shown in Figure S1.

The phase purity and crystal structure of the perovskite films in UV-irradiated PSCs were characterized by X-ray diffraction (XRD) to confirm the component transmutation behind the morphology evolution. Figure 1G exhibits the XRD patterns of perovskite film under UV irradiation for 0, 20, 40, 50, 55, and 65 days. As we can see, all the XRD patterns of perovskite film on TiO_2 ETL under UV exposure within 40 days are almost identical, where the main diffraction peaks centered at 13.99° and 28.19° can be attributed to the (110) and (220) planes of perovskite films. And there is no obvious diffraction peak of PbI_2 centered at 12.60° until UV exposure for 50 days, which is corresponding to the turning point of film morphology. With the extension of illumination time, the proportion of PbI_2 diffraction peak increases rapidly from 5.2% to 51.8% (the intensity ratio compared with the strongest peak) within 15 days. The content of lead iodide (PbI_2) is used to characterize the decomposition degree of perovskite film because PbI_2 is often observed as the final degradation product from lead iodide-based perovskites. Therefore, we can infer that the perovskite film remains unchanged in ∼50 days under such a UV irradiation condition. Afterward, it begins to decompose dramatically in a short time.

Based on the deterioration phenomenon of perovskite films, we investigated the stability of the complete PSCs under continuous UV irradiation (as mentioned above) without encapsulation using an apparatus of stability test. The cells were removed every 24 h to measure the current voltage curves in reverse scan direction under simulated AM 1.5G 100 mW·cm^{-2} irradiance. Figure 1H shows the decay process of device photoelectric conversion efficiency (PCE) calculated from the J-V curves. In the earlier stage, the decay rate is relatively low, wherein the efficiency of PSCs remains 70% of the initial value by ∼50 days. In the later stage, the decay rate suddenly increases, wherein the efficiency drops to ∼1% of the initial value from 50 to 72 days. Apparently, the time node of the PCE abrupt decrease is consistent with the perovskite film decomposition. It can be inferred that the sharp decrease of the device efficiency in the second stage is caused by the rapid decomposition of perovskite absorber. Therefore, we can draw a conclusion that the UV irradiation can lead to two-stage degradation of TiO_2-based PSCs. The earlier decay stage (stage I) and the later decay stage (stage II) constitute the whole degradation process of PSCs. It is also noted that the different decay rates of stage I and stage II indicate different dominating inducements. The underlying trigger factor and the mechanism of the two-stage PSCs UV-degradation process are discussed below.

The Mechanism of Two-Stage UV Degradation

It is well known that there exist inherent oxygen vacancies in TiO_2 ETL, which correspond to Ti^{3+} defects (Ti^{3+}-V_O) with unpaired outer electrons. And the Ti^{3+}-V_O tend to transform into Ti^{4+} defects (Ti^{4+}-V_O)
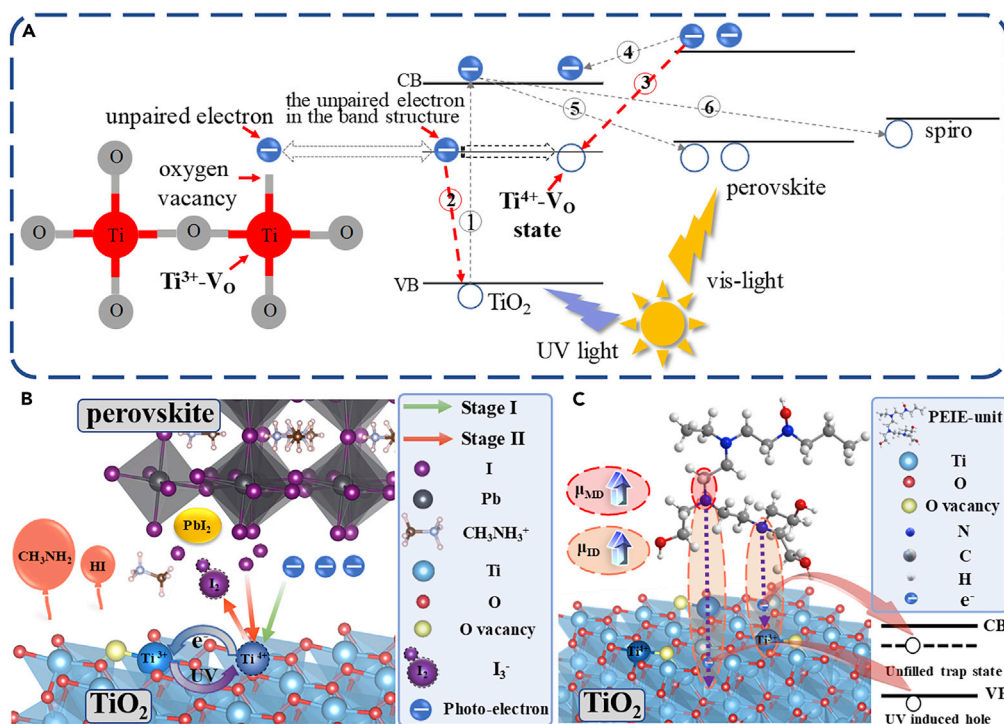
Figure 2. Degradation Mechanism of PSCs under Continuous UV Irradiation
(A) The energy band of TiO_2 ETL and perovskite absorber.
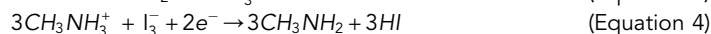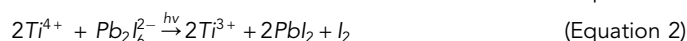(B) The mechanism of PSCs degradation under continuous UV irradiation.
(C) The mechanism of PEIE blocking Ti^{3+}-V_O transformation through donated electrons.

serving as deep traps. Figure 2A shows the detailed generation process of Ti^{4+}-V_O and the carrier recombination channel from the perspective of energy band. In the prepared TiO_2 film, the inherent oxygen vacancies result in Ti^{3+}-V_O with an unpaired electron at ~1 eV below conduction band minimum (Naldoni et al., 2012; Wang et al., 2009). Upon band excitation of TiO_2 induced by UV light, valence band electrons transit to the conduction band (step ①), leaving free holes. Unpaired electrons at the Ti^{3+}-V_O site tend to recombine the holes in the valence band (step ②). This process leaves free electrons in the conduction band and Ti^{4+}-V_O defect states. The Ti^{4+}-V_O states capture photo-generated electrons from perovskite layer (step ③) actively, reverting Ti^{4+}-V_O to Ti^{3+}-V_O, as indicated by the thin green arrow in Figure 2B. And the accumulation of photoelectrons induced by the Ti^{4+}-V_O provide extra electron recombination accesses to holes in the perovskite layer (step ⑤) and HTL layer (step ⑥) (Leijtens et al., 2013), which results in performance decay of PSCs. With the prolongation of UV irradiation time, the concentration of Ti^{4+}-V_O defect states increases continuously, which is resulted from the reaction equilibrium of defects transformation and the increase of Ti^{3+}-V_O (Figure S2) (Xiong et al., 2012; Bennett et al., 2015; Yu et al., 2011; Zhang et al., 2013), leading to the continuous decay of device performance in stage I.

Meanwhile, the UV-excited Ti^{4+}-V_O states can lead to rapid decomposition of perovskite, corresponding to the sharp performance decay. Ti^{4+}-V_O defects provide a large number of oxidizing sites that can oxidize I^- leading to the deposition of I_2 or rather I_3^-, as indicated by the thin red arrow in Figure 2B. Along with the accumulation of polyiodide I_3^-, perovskite films decompose rapidly after a certain delay time under UV illumination, as demonstrated in Figure 1, resulting in the sharp performance decay of PSCs until complete failure. We suppose that it is determined by the kinetics of the decomposition reaction based on the mass action law (Hinrichs and Dreijer-van der Glas, 2015). The decomposition process of perovskite materials under UV irradiation can be described by the following four chemical equations. As is mentioned above, Ti^{3+}-V_O defects in TiO_2 can be converted to oxidizing Ti^{4+}-V_O states after UV exposure (Leijtens et al., 2013), which serve as electron acceptors (Equation 1). And the I^- surrounded by electron acceptors tend to be oxidized turning to I_2, leaving PbI_2 (Abdelmageed et al., 2016; Shlenskaya et al., 2018) (Equation 2). Disengagement of I^- from the lattice caused the collapse of the $Pb_2I_6^{2-}$ octahedral structure,

releasing bound $CH_3NH_3^+$ and causing $CH_3NH_3^+$ migration to the interface between TiO_2 ETL and perovskite layer. Meanwhile, the generated I_2 will combine with the free I^- reversibly (free I^- is abundant in perovskite material [Eames et al., 2015; Haruyama et al., 2015; Azpiroz et al., 2015]), producing polyiodide species I_3^- with strong reduction (Shlenskaya et al., 2018). According to the Pearson hard and soft acid base concept (Shlenskaya et al., 2018; Kim et al., 2012), the neutralization reaction of free soft acid $CH_3NH_3^+$ and free soft base I_3^- happens spontaneously at the interface with the participation of photoelectrons. And this process, shown in Equation 4, generates volatile CH_3NH_2 and HI, exposing PbI_2 product as illustrated in XRD data. Moreover, according to the Equation 2, oxidizing Ti^{4+}-V_O states can trigger the oxidation of I^- circularly excitation, resulting in the accumulation of I_3^- and I_2. Actually, the consumption of $CH_3NH_3^+$ and I^- lead to the deposition of PbI_2, which ultimately completed the perovskite decomposition process. Equation 4 can be recognized as the direct procedure that determines the decomposition rate of perovskite materials. Therefore, the decomposition rate of perovskite material can be approximated by the reaction rate of Equation 4.

$$Ti^{3+} \xrightarrow{h\nu} Ti^{4+} + e^- \qquad \text{(Equation 1)}$$

$$2Ti^{4+} + Pb_2I_6^{2-} \xrightarrow{h\nu} 2Ti^{3+} + 2PbI_2 + I_2 \qquad \text{(Equation 2)}$$

$$I_2 + I^- = I_3^- \qquad \text{(Equation 3)}$$

$$3CH_3NH_3^+ + I_3^- + 2e^- \rightarrow 3CH_3NH_2 + 3HI \qquad \text{(Equation 4)}$$

According to the mass action law (Equation S1), the concentration of $CH_3NH_3^+$ and I_3^- is the main factor that determines the reaction rate of Equation 4. In other words, the accumulation amount of $CH_3NH_3^+$ and I_3^- determines the decomposition rate of perovskite material. The intrinsic free $CH_3NH_3^+$ is negligible (Eames et al., 2015; Haruyama et al., 2015; Azpiroz et al., 2015); the amount of $CH_3NH_3^+$ that participates in the decomposition reaction is proportional to the amount of deposited I_2 and I_3^-. According to the stoichiometry of Equation 2 and Equation 3, it can be concluded: $C_{MA} = 2(C_{I_2} + C_{I_3^-})$, where C_{MA}, C_{I_2}, and $C_{I_3^-}$ are the qualitative concentration of $CH_3NH_3^+$, I_2, and I_3^-, respectively. Combining with the Equation S1, the formula of perovskite decomposition rate can be derived:

$$V = 8kC_{I_3^-}^{\ 4}\left(1 + \frac{1}{KC_{I^-}}\right)^3$$

where V is the decomposition rate of perovskite, k is the chemical reaction rate constant, $C_{I_3^-}$ is the qualitative concentration of I_3^-, K is the chemical equilibrium constant, and C_{I^-} is the qualitative concentration of I^-, which can be considered as a constant. The detailed derivation process of this formula can be seen in Supplemental Information. As shown, the decomposition rate of perovskite is proportional to the fourth power of I_3^- concentration. Consequently, perovskite material will decompose rapidly after a certain I_3^- concentration threshold (Figure S3), corresponding to the lagging sharp decay of device performance in the stage II. The required accumulation time of the threshold concentration of polyiodide I_3^-, namely, the duration time of stage I, is the root of the time difference between stage I and stage II. In addition, we have carried out an intensifying experiment to confirm the origin of the lagging rapid decomposition. External PbI_2, MAI, and I_2 were added into perovskite precursors to prepare PSCs with different perovskite films containing excess suspected decomposition inducers. (Figure S4) This can simulate the reaction environment of the rapid decomposition. Then, we exposed these three groups PSCs to intensive UV irradiation under the above-mentioned test conditions to observe the degradation process. The experimental results demonstrated that the excessive I_2, which could represent the content of I_3^-, led to rapid decomposition of the perovskite film after 5 days UV irradiation (Figure S5). The detailed experimental procedures can be seen in the Supplemental Information.

The transformation of Ti^{3+}-V_O states to Ti^{4+}-V_O states in TiO_2 ETL under UV irradiation serves as the driving force of PSCs UV degradation. In stage I, the photocarrier loss induced by Ti^{4+}-V_O states results in the slow performance decay of PSCs. Afterward, the rapid decomposition of perovskite material initialized by Ti^{4+}-V_O states replaces photocarrier loss to be the domain inducement of degradation, leading to the sharp performance decay in stage II. Therefore, blocking the transformation of Ti^{3+}-V_O states to Ti^{4+}-V_O states becomes the essential approach to inhibit the UV degradation of TiO_2-based PSCs.

PEIE has been proved to be an effective electron donor material (Zhou et al., 2012, 2014; Rasool et al., 2019). Thus, PEIE film can serve as the modified layer of TiO_2 ETL to block the transformation of Ti^{3+}-V_O states. Figure 2C shows the mechanism of PEIE blocking the transformation and passivating the active Ti^{4+}-V_O

trap states. The molecular dipole moment (Rasool et al., 2019) and the interface dipole moment (Zhou et al., 2012; Heimel et al., 2006, 2008; Hong et al., 2010) together result in the electron donation of the amine group. As mentioned above, the UV-excited holes in TiO_2 can capture the outer electron of Ti^{3+}-V_O, turning it into Ti^{4+}-V_O states. Hence, the donated electrons can deplete the UV-excited holes, blocking the transformation of Ti^{3+}-V_O states (Rasool et al., 2019; Zhang et al., 2019; Saracco et al., 2013; Ishii et al., 1999). Moreover, the external electrons can directly passivate Ti^{4+}-V_O trap states, avoiding the capture of photoelectrons and the oxidation of I^-. Therefore, we can infer that PEIE serving as modified layer of TiO_2 ETL can enhance the UV resistance of PSCs significantly.
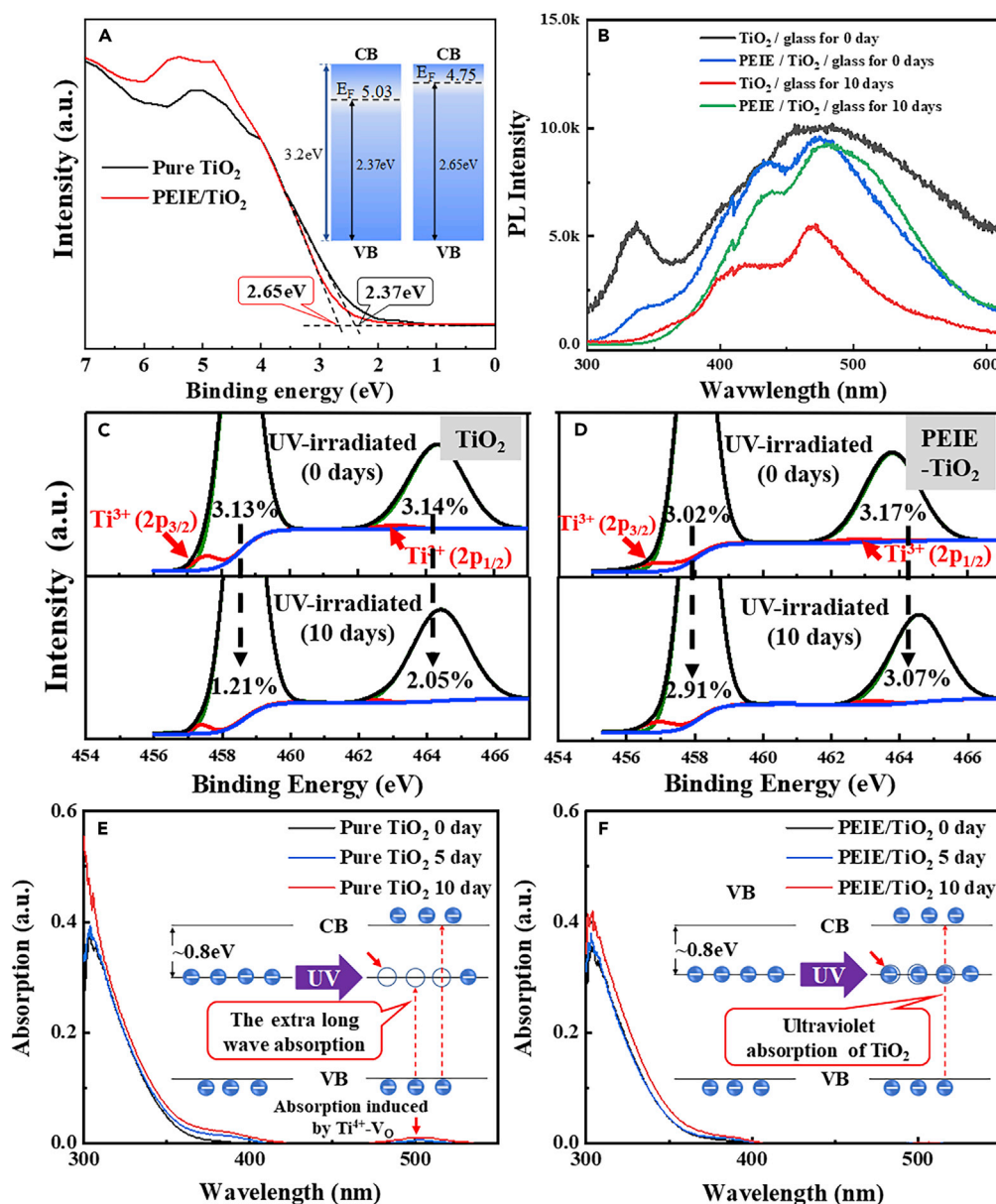
Evidence for the Transformation of Ti^{3+}-V_O States and the Blocking Effect of PEIE

We prepared planar TiO_2-based PSCs with and without PEIE modified layer on TiO_2 ETL to explore the transformation of Ti^{3+}-V_O states and the blocking effect of PEIE layer. The PSCs construction and the molecular structure of PEIE are shown in Figure S6A. The detailed fabrication procedures of the PEIE-modified PSCs are shown in the Experimental section of Supplemental Information. Figure S6B displays the X-ray photoelectron spectroscopy (XPS) results of the PEIE-TiO_2 and pure-TiO_2 films deposited on FTO/glass. The presence of PEIE can be verified by the N1s peak at 399.8 eV, which is negligible in pure-TiO_2. The surface morphology of PEIE-modified TiO2 ETL was measured by atomic force microscopy (AFM), as shown in Figure S7. The transformation of Ti^{3+}-V_O defect states is discussed below.

In order to confirm the blocking effect of PEIE on the transformation of Ti^{3+}-V_O states, which is achieved by the donated electrons, the Fermi level of TiO_2 films with and without PEIE layer were estimated by UV photoelectron spectroscopy (UPS) patterns through the tangential extension method. As shown in Figure 3A, the point at which the tangent line intersects the horizontal line on the x-coordinate in UPS curves represents the distance from the valence band maximum to the Fermi energy level. The energy distance of pure-TiO_2 is 2.37 eV compared with 2.65 eV of PEIE-TiO_2, which confirmed the 0.28-eV increment in Fermi level of PEIE-TiO_2. This result proves that external electrons can be injected into the TiO_2 efficiently from the PEIE layer by processes such as tunneling or thermionic injection (Kim et al., 2012). The donated electrons tend to deplete the UV exited holes.

The defect states density in TiO_2 ETL under UV irradiation was characterized by steady photoluminescence (PL) measurement. The samples of TiO_2 films with and without PEIE layer on glass substrate, which had been exposed in UV irradiation for 0, 10 days in an argon-filled glovebox, were operated in liquid nitrogen at 80 K for steady PL measurement. (The dominant recombination processes of anatase TiO_2 at room temperature are nonradiative [Knorr et al., 2008; Li et al., 2016].) As shown in Figure 3B, the PL spectrum reveals a broad emission centered at around 480 nm. And the corresponding radiation energy is 2.58 eV, demonstrating that the photoluminescence is mainly produced by Ti^{3+} defect level ($\sim$2.5 eV above the valence band maximum) at 80 K. Under UV irradiation for 10 days, the PL intensity of pure-TiO_2 film is declined markedly. In general, the PL intensity of TiO_2 film is related to the concentration of defect states that can serve as the nonradiative carrier recombination centers. Hence, the lower PL intensity of the irradiated pure-TiO_2 film (the red line) indicates that the density of defect states in pure-TiO_2 increased obviously after UV irradiation. However, the PL intensity of PEIE-TiO_2 film is almost unchanged, demonstrating that the PEIE modification layer on TiO_2 can significantly suppress the UV-induced defect states.

To confirm the nature source of UV-induced defect states, the TiO_2 films on glass with and without PEIE modification layer under UV irradiation for 0 and 10 days was also measured by XPS, as depicted in Figures S8A and S8B. The peak located at 458.7 eV is assigned to the Ti ($2p_{3/2}$), and the peak located at 464.3 eV is assigned to Ti ($2p_{1/2}$). For the 458.7 eV peak, two titanium containing components are clearly resolved through peak fitting by Origin. The main peak at 458.7 eV (marked by the green line) is assigned to the lattice Ti^{4+} ($2p_{3/2}$), and the shoulder peak at $\sim$457.5 eV (marked by the red line) is assigned to the oxygen vacancy-Ti^{3+} ($2p_{3/2}$) (Sandell et al., 2003; Jiang et al., 2012). This $\sim$1.2-eV energy difference is consistent with previous reports (Wang et al., 2009; Pan et al., 2013; Wetzelaer et al., 2015). It is well known that the area of characteristic peaks can indicate the content of corresponding elements. Through the peak area integral calculation, as shown, the content of Ti^{3+}($2p_{3/2}$) in pure-TiO_2 film was reduced from 3.13% to 1.21% after 10 days of UV exposure, as indicated in Figure 3C. This occurs when unpaired electrons in Ti^{3+}-V_O recombine with holes in valence band excited by UV radiation, indicating the transformation of Ti^{3+}-V_O states to Ti^{4+}-V_O states. Moreover, the 464.3 eV peak, which corresponds to Ti ($2p_{1/2}$), shows a similar phenomenon. Therefore, it can be concluded that the generated defect states in TiO_2 under UV

Figure 3. Evidence of the Ti³⁺-Vₒ States Transformation and the Blocking Effect of PEIE

(A) UPS measurements of pure-TiO$_2$ and PEIE-TiO$_2$ films on glass substrate.

(B) Low temperature (80 K) steady-state PL spectra (250-nm xenon lamp excitation) of pure-TiO$_2$ and PEIE-TiO$_2$ film on glass substrate under UV irradiation for 0 and 10 days.

(C and D) XPS Ti(2p) spectra of pure-TiO$_2$ film (C) and PEIE-TiO$_2$ film (D) on glass under UV irradiation for 0 and 10 days.

(E and F) UV-visible absorption spectra of (E) pure-TiO$_2$ film and (F) PEIE-TiO$_2$ film under continuous UV irradiation for 0, 5, and 10 days.

See also Figure S8.

irradiation are Ti^{4+}-V$_O$ states, which are transformed from Ti^{3+}-V$_O$ states. Figure 3D shows the Ti^{3+}-V$_O$ decrement of PEIE-TiO$_2$ from 3.02% to 2.91% for Ti^{3+}(2p$_{3/2}$) and from 3.17% to 3.07% for Ti^{3+} (2p$_{1/2}$) under UV irradiation for 10 days, which is significantly less than pure-TiO$_2$, demonstrating the effective blocking effect of PEIE on Ti^{3+}-V$_O$ transformation, consistent with PL result.

Furthermore, the UV-vis spectra were obtained to measure the generation of Ti^{4+}-V$_O$ states. As the inserted diagram in Figure 3E shows, the Ti^{3+}-V$_O$ defect states with unpaired electrons have no significant effect on the
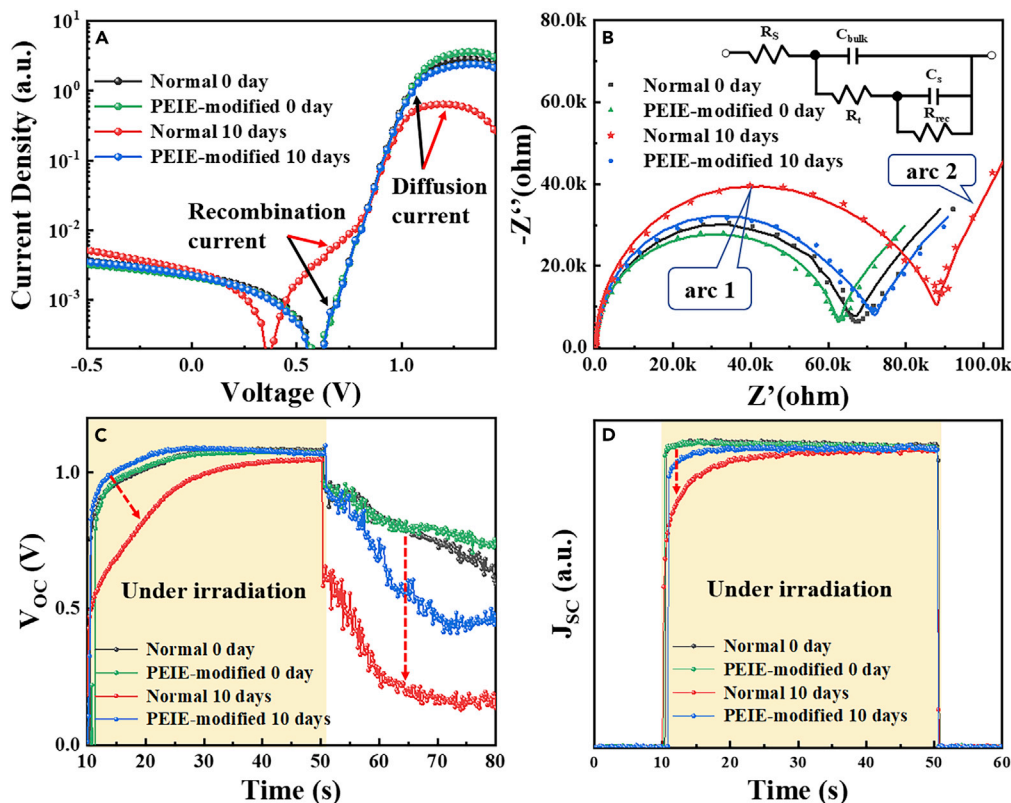
Figure 4. Performance Decrease of Perovskite Solar Cells

(A) The evolution of dark current characteristic curves.

(B) The evolution of electrochemical impedance.

(C) The evolution of V_{OC} decay.

(D) The evolution of Transient J_{SC} (normalized at maxima). These PSCs were exposed to UV irradiation in an argon-filled glovebox at room temperature. Complex impedance plot for PSCs measured in dark condition at short circuit conditions.

absorption spectrum of TiO_2 film. Under UV irradiation, Ti^{3+}-V_O states tend to transform into Ti^{4+}-V_O states leaving unfilled defect energy levels in TiO_2, which can cause long wave absorption of TiO_2 films. Figures 3E and 3F exhibit the UV-vis absorption spectra of TiO_2 films with and without PEIE modification layer on glass substrate under UV illumination for 0, 5, and 10 days. As seen, after 5 and 10 days UV exposure, the pure-TiO_2 film generated a weak defect absorption peak at the wavelength of ~500 nm, which corresponds to the Ti^{4+}-V_O states at ~1 eV below the conduction band minimum. This result confirms the presence of Ti^{4+}-V_O states in TiO_2 transformed from Ti^{3+}-V_O after UV irradiation. As discussed earlier, the PEIE layer can inject electrons into the TiO_2 film filling the UV-induced defect states, which is the passivation process of Ti^{4+}-V_O states, as is depicted in the inserted image in Figure 3F. This process can suppress the defect absorption effectively, so there is no obvious defect peak in the absorption spectrum of PEIE-TiO_2 films.

Performance Decrease Induced by Ti^{4+}-V_O States

In an attempt to explore the effect of Ti^{4+}-V_O trap states on device performance, we have performed multiple electrical tests for PSCs after 0 and 10 days UV exposure. The dark current curves of the PSCs based on pure-TiO_2 ETL and PEIE-TiO_2 ETL are characterized and shown in Figure 4A. As seen, the dark current at the low voltage scale, mainly determined by the recombination current, is higher in UV-degraded PSC with pure-TiO_2 ETL (the red line), whereas the current after the threshold voltage, mainly determined by the diffusion current, is lower. As the recombination of the PSCs is evidenced to be governed by the trap states (Song et al., 2016; Wetzelaer et al., 2015), the higher recombination current in the degraded PSC indicates more severe recombination induced by Ti^{4+}-V_O states, reflecting the photocarrier loss. And the lower diffusion current in the UV-degraded PSC corresponds to the high resistance to photoelectron transport raised by Ti^{4+}-V_O states. On the contrary, the PSCs based on PEIE-TiO_2 ETL have no apparent performance

variation in dark current curve after UV exposure, demonstrating that the PEIE layer does reduce the carrier recombination caused by Ti^{4+}-V_O state and enhance electron transport.

The interfacial electron transfer between ETL and perovskite layer was investigated by electrochemical impedance spectrum (EIS) to observe the degradation caused by UV-induced Ti^{4+}-V_O states. EIS is used as an effective tool to certify the charge transport and recombination processes. Figure 4B shows the Nyquist plots of PSCs with pure-TiO_2 ETL and PEIE-TiO_2 ETL under UV irradiation for 0 and 10 days measured at 0 V bias in dark. R_t (transport resistance) and R_{rec} (recombination resistance) can be obtained by fitting Nyquist plots using the equivalent circuit shown in Figure 4B inserted image. The lower frequency circle (arc 2) is related to the charge recombination, and the higher frequency circle (arc 1) belongs to charge transfer at ETL/perovskite interfaces because the perovskite/HTL interfaces were identical in both cases. For the UV-degraded PSCs based on pure-TiO_2, the R_{rec} is significantly smaller than the fresh PSCs, whereas the transfer resistance R_t is larger (the fitting values are shown in the Table S1). This consequence indicates that UV-induced Ti^{4+}-V_O states can increase photocarrier recombination and transfer resistance, leading to the performance decrease. However, the R_{rec} and R_t of the PSCs modified with PEIE layer have no remarkable change after UV exposure, consistent with dark current data.

Open circuit voltage decay (OCVD) was performed to study the effect of Ti^{4+}-V_O states on electron extraction. As shown in Figure 4C, the V_{OC} decay curves of UV-degraded PSCs with pure-TiO_2 ETL (the red line) exhibit lower voltage than the fresh one, which correspond to the accumulation of photocarrier at the interface between the absorb layer and transport layer. At the initial descent point (immediately after the irradiation off) of the V_{OC} decay curve, the decrease of V_{OC} is obviously faster in the UV-degraded PSCs compared with the fresh one. And the voltage increment of the UV-degraded PSC immediately after the irradiation on is slower. In our previous work, we show that the more severe decay in OCVD curves corresponds to the presence of more trap states and the poor performance of PSCs (Song et al., 2015, 2016; Cui et al., 2015), which are consistent with the case of UV-degraded PSCs. These results illustrate that the UV-induced Ti^{4+}-V_O states, proved earlier, can lead to serious electron recombination and poor electron extraction, resulting in photocarrier loss. Furthermore, the UV-induced Ti^{4+}-V_O states also lead to the slow response of the photocurrent. As shown in Figure 4D, J_{SC} of the UV-degraded PSCs with pure-TiO_2 ETL increases more slowly after the light on than that of the fresh PSCs, further proving the photocarrier loss caused by UV-induced Ti^{4+}-V_O states. The V_{OC} decay curve and J_{SC} increase curve of UV-degraded PSCs with PEIE-TiO_2 ETL (the blue line) retain slow decay and fast increase, respectively. This proves that the PEIE layer can effectively reduce the interface carrier recombination, indicating the improved UV stability of modified PSCs.

Ti^{4+}-V_O states can also trigger the decomposition of perovskite film causing performance decrease. After 50 days of UV irradiation, the perovskite film began to decompose rapidly. This can be proved by the XRD patterns and SEM images in Figures 1C–1G. Notably, the PEIE-modified layer on TiO_2 ETL can effectively inhibit the decomposition of perovskite film. Figure S9A and S9B show the XRD spectra of the perovskite films in normal and PEIE-modified PSCs under UV irradiation for 0, 20, 40, 50, 55, and 65 days in an argon-filled glovebox at room temperature. As mentioned above, the perovskite films in normal PSCs decomposed significantly after 50 days UV exposure. However, there is no apparent decomposition of the perovskite films in PEIE-modified PSCs for 65 days UV irradiation. Moreover, the morphology evolution of perovskite films is depicted in Figure S10. The broken perovskite films in normal PSCs after 50 days UV exposure indicate the serious decomposition. But the PEIE-modified samples exhibit no obvious morphology change. In conclusion, perovskite films decompose seriously after 50 days, but the introduction of the PEIE modified layer can effectively suppress the decomposition process, suggesting the excellent UV resistance.

The Improved Device Stability

The photovoltaic performance of the perovskite solar cells consisting of pure-TiO_2 ETL and PEIE-modified TiO_2 ETL was measured under AM 1.5G, 1 sun illumination in reverse direction. Figure 5A exhibits the current-voltage plots of the devices with (red) and without (black) PEIE modification layer. The detailed photovoltaic parameters of short-circuit current density (J_{SC}), open-circuit voltage (V_{OC}), fill factor (FF), and photoelectric conversion efficiency values (PCE) are summarized in the inserted table. The best device among the normal PSCs achieved a PCE of 20.03% with a J_{SC} of 23.96 mA·cm^{-2}, a V_{OC} of 1.100 V, and a fill factor (FF) of 76%. And the PEIE-modified device achieved a PCE of 20.51% with a J_{SC} of 24.33 mA·cm^{-2}, a V_{OC} of 1.109 V, and a fill factor (FF) of 76%. The corresponding external quantum efficiency (EQE) and integrated short-circuit current density are presented in Figure 5B. The EQE measurements showing a high
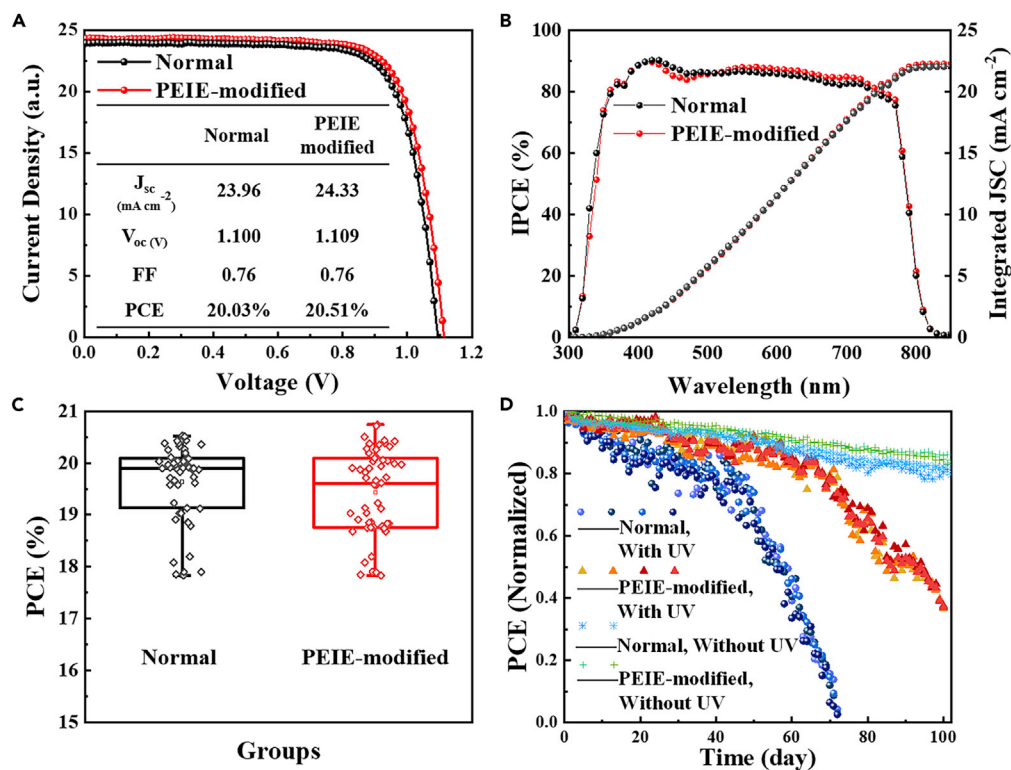
Figure 5. PSCs Performance and Stability

(A) J-V curves of the best PSCs with (red) and without (black) PEIE modification layer under AM 1.5G 100 mW·cm^{-2} illumination. Inset: Device performance parameters calculated from the curves.

(B) External quantum efficiency (EQE) spectrum of the normal and PEIE-modified PSCs.

(C) Device performance distribution for 55 normal devices and 55 PEIE-modified devices in one batch.

(D) The normalized PCE decay of the normal and PEIE-modified PSCs under 254-nm UV irradiation with an intensity of 50 mW·cm^{-2} at room temperature in an argon-filled glovebox.

photo-to-current conversion over 90% at 430 nm indicates good utilization of photons in the short-wavelength (360–560 nm) region of sunlight. And the integrated current density of 22.08 and 22.30 mA·cm^{-2} for normal and PEIE-modified devices, respectively, is in good agreement with J-V results. In addition, both normal and PEIE-modified PSCs show a narrow distribution of PCE with the median value of 19.8% and 19.6%, as depicted in Figure 5C. Notably, the introduction of PEIE has slightly reduced the repeatability of device performance. These performance results prove a fact that the introduction of PEIE modification layer has no significant impact on the photoelectric performance of PSCs; on the contrary, it even has the potential to improve the device efficiency due to the enhanced electron extraction of TiO$_2$ ETL (Zhou et al., 2012, 2014). This can also be demonstrated by PL spectrums of perovskite film, as shown in Figure S11. In addition, the introduction of PEIE layer did not improve the hysteresis effect of PSCs, which was still obvious, as shown in Figure S12.

The more important goal of this work is to investigate the effect of blocking transformation by PEIE on UV stability. Here, we used UV lamp (λ = 254 nm) to irradiate the PSCs at room temperature in an argon-filled glovebox. Figure 5D displays the efficiency decay curves of the PSCs with and without PEIE modification layer on TiO$_2$ ETL under UV irradiation for 100 days. As a comparison, the decay curves of normal PSCs and PEIE modified PSCs without UV irradiation are also exhibited in Figure 5D. Significant two-stage UV degradation of all the PSCs is clearly observed. However, the efficiency decay of the PEIE-modified PSCs is slower. On the whole, the PEIE-modified PSCs remained ~75% of its initial efficiency when the normal PSCs failed completely at 75 days under continuous intensive UV irradiation. Furthermore, in stage I, the decay rate of PEIE-modified PSCs is reduced from 0.60 to 0.42, when compared with normal PSCs. In stage II, the decay rate of PEIE-modified PSCs is reduced from 3.50 to 2.33. (This rate value is calculated by the equation: $r = \frac{\Delta E}{t}$, where r is decay rate, ΔE is percentage decrease of efficiency, and t is irradiation time).

In addition, the time threshold of rapid perovskite decomposition is postponed from 50 to 70 days. In this work, a large number of devices (including normal PSCs and PEIE-modified PSCs) were monitored under the same UV irradiation condition. The error of the transition point in decay curves is ±5 days. The outcomes suggest that blocking the Ti^{3+} transformation by PEIE-modified layer is an effective way to enhance the UV stability of the TiO_2-based PSCs.

CONCLUSION

In summary, a two-stage UV degradation process of TiO_2-based PSCs was discovered. The Ti^{4+}-V_O states transformed from inherent Ti^{3+}-V_O under UV irradiation cause the photocarrier loss, resulting in the first slower decay process (stage I), whereas the rapid decomposition of perovskite film after a period of UV exposure triggered by Ti^{4+}-V_O states leads to the second sharp performance decay (stage II). In essence, the transformation of Ti^{3+}-V_O states drives the two-stage UV degradation. Based on this mechanism, a universal method was proposed that blocking the transformation of Ti^{3+}-V_O states inhibits the UV degradation of TiO_2-based PSCs. Herein, PEIE-modified layer was introduced to block the transformation enhancing the UV stability significantly. The two-stage UV-degradation mechanism can help address the UV instability issue of TiO_2-based PSCs, offering a promising path to achieve high-efficiency devices with excellent UV resistance for commercialization.

Limitations of the Study

In this study, an ultrathin polymer interfacial layer (PEIE) is introduced to improve the UV stability of PSCs. However, this layer may not be uniform and compact, which limits its UV resistance and the repeatability of device performance. The deposition process of the PEIE layer should be further optimized.

METHODS

All methods can be found in the accompanying Transparent Methods supplemental file.

DATA AND CODE AVAILABILITY

All data needed to evaluate the conclusions in the paper are present in the paper and/or the Supplemental Information. Additional data related to this paper may be requested from M.L. (mcli@ncepu.edu.cn).

SUPPLEMENTAL INFORMATION

Supplemental Information can be found online at https://doi.org/10.1016/j.isci.2020.101013.

AUTHOR CONTRIBUTIONS

M.L. and J.J. conceived the idea and designed the experiments. J.J. and X.L. contributed equally to this work. J.J. and X.L. fabricated the devices and conducted stability test. H.J., M.D, B.L., and H.H performed the optical characterizations (XPS, steady-state PL, XRD, and absorption spectrums) of the TiO_2 ETL. H.J., H.H., D.W., and Y.L. performed the electrical characterizations (dark current, EIS, and OCVD) of the PSCs. All authors contributed to the data analysis and commented on the manuscript.

DECLARATION OF INTERESTS

The authors declare no competing interests.

REFERENCES

Abdelmageed, G., Jewell, L., Hellier, K., Seymour, L., Luo, B., Bridges, F., Zhang, J.Z., and Carter, S. (2016). Mechanisms for light induced degradation in MAPbI$_3$ perovskite thin films and solar cells. Appl. Phys. Lett. *109*, 233905.

Ahn, N., Kwak, K., Jang, M.S., Yoon, H., Lee, B.Y., Lee, J.-K., Pikhitsa, P.V., Byun, J., and Choi, M. (2016). Trapped charge-driven degradation of perovskite solar cells. Nat. Commun. *7*, 13422.

Aristidou, N., Sanchez-Molina, I., Chotchuangchutchaval, T., Brown, M., Martinez, L., Rath, T., and Haque, A.A. (2015). The role of oxygen in the degradation of methylammonium lead trihalide perovskite photoactive layers. Angew. Chem. Int. Ed. *54*, 8208–8212.

Azpiroz, J.M., Mosconi, E., Bisquert, J., and De Angelis, F. (2015). Defect migration in methylammonium lead iodide and its role in perovskite solar cell operation. Energy Environ. Sci. *8*, 2118–2127.

Bai, S., Da, P., Li, C., Wang, Z., Yuan, Z., Fu, F., Kawecki, M., Liu, X., Sakai, N., and Wang, J.T.-W. (2019). Planar perovskite solar cells with long-term stability using ionic liquid additives. Nature *571*, 245–250.

Bennett, T., Adnan, R.H., Alvino, J.F., Kler, R., Golovko, V.B., Metha, G.F., and Andersson, G.G. (2015). Effect of gold nanoclusters on the production of Ti^{3+} defect sites in titanium dioxide nanoparticles under ultraviolet and soft X-ray radiation. J. Phys. Chem. C *119*, 11171–11177.

Best, NREL., 2019. https://www.nrel.gov/pv/assets/pdfs/best-research-cell-efficiencies.20191106.pdf.

Bryant, D., Aristidou, N., Pont, S., Sanchez-Molina, I., Chotchunangatchaval, T., Wheeler, S., Durrant, J.R., and Haque, S.A. (2016). Light and oxygen induced degradation limits the operational stability of methylammonium lead triiodide perovskite solar cells. Energy Environ. Sci. *9*, 1655–1660.

Cui, P., Fu, P., Wei, D., Li, M., Song, D., Yue, X., Li, Y., Zhang, Z., Li, Y., and Mbengue, J.M. (2015). Reduced surface defects of organometallic perovskite by thermal annealing for highly efficient perovskite solar cells. RSC Adv. *5*, 75622–75629.

Cui, P., Wei, D., Ji, J., Song, D., Li, Y., Liu, X., Huang, J., Wang, T., You, J., and Li, M. (2017). Highly efficient electron-selective layer free perovskite solar cells by constructing effective p-n heterojunction. Solar RRL *1*, 1600027.

Cui, P., Wei, D., Ji, J., Huang, H., Jia, E., Dou, S., Wang, T., Wang, W., and Li, M. (2019). Planar p-n homojunction perovskite solar cells with efficiency exceeding 21.3%. Nat. Energy *4*, 150–159.

Eames, C., Frost, J.M., Barnes, P.R., O'regan, B.C., Walsh, A., and Islam, M.S. (2015). Ionic transport in hybrid lead iodide perovskite solar cells. Nat. Commun. *6*, 7497.

Gottesman, R., Lopez-Varo, P., Gouda, L., Jimenez-Tejada, J.A., Hu, J., Tirosh, S., Zaban, A., and Bisquert, J. (2016). Dynamic phenomena at perovskite/electron-selective contact interface as interpreted from photovoltage decays. Chem *1*, 776–789.

Han, G.S., Chung, H.S., Kim, B.J., Kim, D.H., Lee, J.W., Swain, B.S., Mahmood, K., Yoo, J.S., Park, N.-G., and Lee, J.H. (2015). Retarding charge recombination in perovskite solar cells using ultrathin MgO-coated TiO$_2$ nanoparticulate films. J. Mater. Chem. A. *3*, 9160–9164.

Haruyama, J., Sodeyama, K., Han, L., and Tateyama, Y. (2015). First-principles study of ion diffusion in perovskite solar cell sensitizers. J. Am. Chem. Soc. *137*, 10048–10051.

Heimel, G., Romaner, L., Brédas, J.L., and Zojer, E. (2006). Interface energetics and level alignment at covalent metal-molecule junctions: π-conjugated thiols on gold. Phys. Rev. Lett. *96*, 196806.

Heimel, G., Romaner, L., Zojer, E., and Bredas, J.-L. (2008). The interface energetics of self-assembled monolayers on metals. Acc. Chem. Res. *41*, 721–729.

Hinrichs, W., and Dreijer-van der Glas, S. (2015). Physical Chemistry (Springer International Publishing).

Hong, L., Paramonov, P., and Bredas, J.L. (2010). Theoretical study of the surface modification of indium tin oxide with trifluorophenyl phosphonic acid molecules: impact of coverage density and binding geometry. J. Mater. Chem. *20*, 2630–2637.

Ishii, H., Sugiyama, K., Ito, E., and Seki, K. (1999). Energy level alignment and interfacial electronic structures at organic/metal and organic/organic interfaces. Adv. Mater. *11*, 605–625.

Ito, S., Tanaka, S., Manabe, K., and Nishino, H. (2014). Effects of surface blocking layer of Sb$_2$S$_3$ on nanocrystalline TiO$_2$ for CH$_3$NH$_3$PbI$_3$ perovskite solar cells. J. Phys. Chem. C *118*, 16995–17000.

Jeon, N.J., Noh, J.H., Yang, W.S., Kim, Y.C., Ryu, S., Seo, J., and Seok, S.I. (2015). Compositional engineering of perovskite materials for high-performance solar cells. Nature *517*, 476–480.

Jiang, X., Zhang, Y., Jing, J., Rong, Y., and Pan, C. (2012). Characterization of oxygen vacancy associates within hydrogenated TiO$_2$: a positron annihilation study. J. Phys. Chem. C *116*, 22619–22624.

Kim, S.H., Kim, E.M., Lee, C.M., Dong, W.K., Lim, S.T., Sohn, M.H., and Jeong, H.J. (2012). Synthesis of PEG-iodine-Capped gold nanoparticles and their Contrast enhancement in in vitro and in vivo for X-ray/CT. J. Nanomater. *2012*, 344–353.

Kim, H., Lim, K.G., and Lee, T.W. (2016). Planar heterojunction organometal halide perovskite solar cells: roles of interfacial layers. Energy Environ. Sci. *9*, 12–30.

Knorr, F.J., Mercado, C.C., and McHale, J.L. (2008). Trap-state distributions and carrier transport in pure and mixed-phase TiO$_2$: influence of contacting solvent and interphasial electron transfer. J. Phys. Chem. C *112*, 12786–12794.

Lee, S.-W., Kim, S., Bae, S., Cho, K., Chung, T., Hwang, J.-K., Song, I., Lee, W., Park, S., and Jung, J. (2018). Enhanced UV stability of perovskite solar cells with a SrO interlayer. Org. Electron. *63*, 343–348.

Leijtens, T., Eperon, G.E., Pathak, S., Abate, A., Lee, M.M., and Snaith, H.J. (2013). Overcoming ultraviolet light instability of sensitized TiO$_2$ with meso-superstructured organometal tri-halide perovskite solar cells. Nat. Commun. *4*, 2885.

Li, Y., Cooper, J.K., Liu, W., Sutter-Fella, C.M., Amani, M., Beeman, J.W., Javey, A., Ager, J.W., Liu, Y., and Toma, F.M. (2016). Defective TiO$_2$ with high photoconductive gain for efficient and stable planar heterojunction perovskite solar cells. Nat. Commun. *7*, 12446.

Naldoni, A., Allieta, M., Santangelo, S., Marelli, M., Fabbri, F., Cappelli, S., Bianchi, C.L., Psaro, R., and Dal Santo, V. (2012). Effect of nature and location of defects on bandgap narrowing in black TiO$_2$ nanoparticles. J. Am. Chem. Soc. *134*, 7600–7603.

Niu, G., Guo, X., and Wang, L. (2015). Review of recent progress in chemical stability of perovskite solar cells. J. Mater. Chem. A. *3*, 8970–8980.

Pan, X., Yang, M.-Q., Fu, X., Zhang, N., and Xu, Y.-J. (2013). Defective TiO$_2$ with oxygen vacancies: synthesis, properties and photocatalytic applications. Nanoscale *5*, 3601–3614.

Rasool, S., Khan, N., Jahankhan, M., Kim, D.H., Ho, T.T., Do, L.T., Song, C.E., Lee, H.K., Lee, S.K., and Lee, J.C. (2019). Amine-based interfacial engineering in solution-processed organic and perovskite solar cells. ACS Appl. Mater. Inter. *11*, 16785–16794.

Sandell, A., Andersson, M.P., Johansson, K.J., Karlsson, P.G., and Uvdal, P. (2003). Metalorganic chemical vapor deposition of anatase titanium dioxide on Si: modifying the interface by pre-oxidation. Surf. Sci. *530*, 63–70.

Saracco, E., Bouthinon, B., Verilhac, J.M., Celle, C., Chevalier, N., Mariolle, D., Dhez, O., and Simonato, J.P. (2013). Work function tuning for high-performance solution-processed organic photodetectors with inverted structure. Adv. Mater. *25*, 6534–6538.

Shin, S.S., Yeom, E.J., Yang, W.S., Hur, S., Kim, M.G., Im, J., Seo, J., Noh, J.H., and Seok, S.I. (2017). Colloidally prepared La-doped BaSnO$_3$ electrodes for efficient, photostable perovskite solar cells. Science *356*, 167–171.

Shlenskaya, N.N., Belich, N.A., Grätzel, M., Goodilin, E.A., and Tarasov, A.B. (2018). Light-induced reactivity of gold and hybrid perovskite as a new possible degradation mechanism in perovskite solar cells. J. Mater. Chem. A. *6*, 1780–1786.

Song, D., Cui, P., Wang, T., Wei, D., Li, M., Cao, F., Yue, X., Fu, P., Li, Y., and He, Y. (2015). Managing carrier lifetime and doping property of lead halide perovskite by postannealing processes for highly efficient perovskite solar cells. J. Phys. Chem. C *119*, 22812–22819.

Song, D., Ji, J., Li, Y., Li, G., Li, M., Wang, T., Wei, D., Cui, P., He, Y., and Mbengue, J.M. (2016). Degradation of organometallic perovskite solar cells induced by trap states. Appl. Phys. Lett. *108*, 093901.

Tsai, H., Asadpour, R., Blancon, J.-C., Stoumpos, C.C., Durand, O., Strzalka, J.W., Chen, B., Verduzco, R., Ajayan, P.M., and Tretiak, S. (2018). Light-induced lattice expansion leads to high-efficiency perovskite solar cells. Science *360*, 67–70.

Wan, F., Qiu, X., Chen, H., Liu, Y., Xie, H., Shi, J., Huang, H., Yuan, Y., Gao, Y., and Zhou, C. (2018). Accelerated electron extraction and improved UV stability of TiO₂ based perovskite solar cells by SnO₂ based surface passivation. Org. Electron. *59*, 184–189.

Wang, J., Tafen, D.N., Lewis, J.P., Hong, Z., Manivannan, A., Zhi, M., Li, M., and Wu, N. (2009). Origin of photocatalytic activity of nitrogen-doped TiO₂ nanobelts. J. Am. Chem. Soc. *131*, 12290–12297.

Wang, L., Zhou, H., Hu, J., Huang, B., Sun, M., Dong, B., Zheng, G., Huang, Y., Chen, Y., and Li, L. (2019). A Eu³⁺-Eu²⁺ ion redox shuttle imparts operational durability to Pb-I perovskite solar cells. Science *363*, 265–270.

Wei, J., Li, H., Zhao, Y., Zhou, W., Fu, R., Pan, H., and Zhao, Q. (2016). Flexible perovskite solar cells based on the metal-cinsulator-semiconductor structure. Chem. Commun. *52*, 10791–10794.

Wei, J., Guo, F., Liu, B., Sun, X., Wang, X., Yang, Z., Xu, K., Lei, M., Zhao, Y., and Xu, D. (2019a). UV-inert ZnTiO₃ electron selective layer for photostable perovskite solar cells. Adv. Energy Mater. *9*, 1901620.

Wei, D., Huang, H., Cui, P., Ji, J., Dou, S., Jia, E., Sajid, S., Cui, M., Chu, L., and Li, Y. (2019b). Moisture-tolerant supermolecule for the stability enhancement of organic-inorganic perovskite solar cells in ambient air. Nanoscale *11*, 1228–1235.

Wetzelaer, G.J.A.H., Scheepers, M., Sempere, A.M., Momblona, C., Ávila, J., and Bolink, H.J. (2015). Trap-assisted non-radiative recombination in organic-inorganic perovskite solar cells. Adv. Mater. *27*, 1837–1841.

Xiong, L.-B., Li, J.-L., Yang, B., and Yu, Y.J. (2012). Ti³⁺ in the surface of titanium dioxide: generation, properties and photocatalytic application. Nanomater *9*, 831524.

Yang, S., Chen, S., Mosconi, E., Fang, Y., Xiao, X., Wang, C., Zhou, Y., Yu, Z., Zhao, J., and Gao, Y. (2019). Stabilizing halide perovskite surfaces for solar cell operation with wide-bandgap lead oxysalts. Science *365*, 473–478.

Yu, Y., Wu, K., and Wang, D. (2011). Dye-sensitized solar cells with modified TiO₂ surface chemical states: the role of Ti³⁺. Appl. Phys. Lett. *99*, 192104.

Zhang, X., Tian, H., Wang, X., Xue, G., Tian, Z., Zhang, J., Yuan, S., Yu, T., and Zou, Z. (2013). The role of oxygen vacancy-Ti³⁺ states on TiO₂ nanotubes' surface in dye-sensitized solar cells. Mater. Lett. *100*, 51–53.

Zhang, B., Song, Z., Jin, J., Bi, W., Li, H., Chen, C., Dai, Q., Xu, L., and Song, H. (2019). Efficient rare earth Co-doped TiO₂ electron transport layer for high-performance perovskite solar cells. J. Colloid Interf. Sci. *533*, 14–21.

Zhou, Y., Fuentes-Hernandez, C., Shim, J., Meyer, J., Giordano, A.J., Li, H., Winget, P., Papadopoulos, T., Cheun, H., and Kim, J. (2012). A universal method to produce low-work function electrodes for organic electronics. Science *336*, 327–332.

Zhou, H., Chen, Q., Li, G., Luo, S., Song, T.-b., Duan, H.-S., Hong, Z., You, J., Liu, Y., and Yang, Y. (2014). Interface engineering of highly efficient perovskite solar cells. Science *345*, 542–546.

Supplemental Information

Two-Stage Ultraviolet Degradation

of Perovskite Solar Cells Induced

by the Oxygen Vacancy-Ti^{4+} States

Jun Ji, Xin Liu, Haoran Jiang, Mingjun Duan, Benyu Liu, Hao Huang, Dong Wei, Yingfeng Li, and Meicheng Li
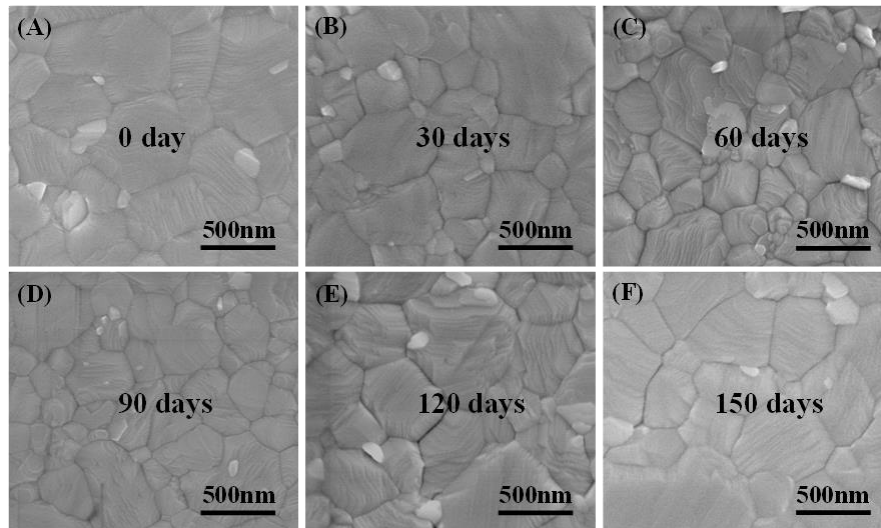
Supplemental Figures

Figure S1. The SEM images of perovskite film deposided on glass substrate for 0, 30, 60, 90, 120, 150 days in argon-filled glovebox, related to Figure 1.
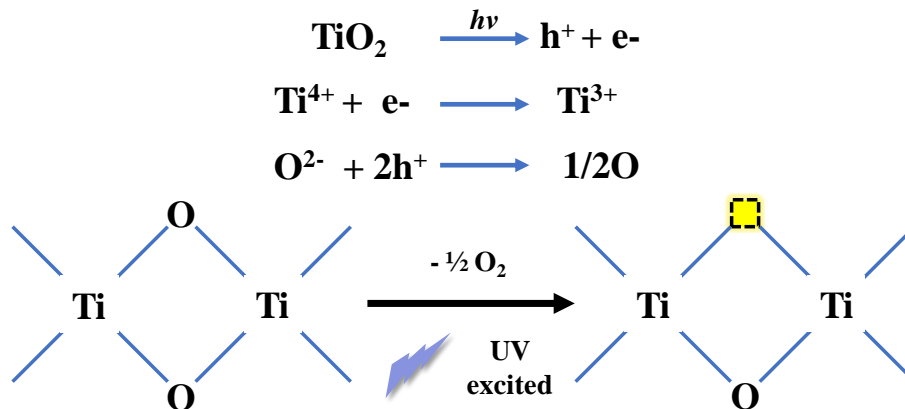
$$TiO_2 \xrightarrow{hv} h^+ + e^-$$

$$Ti^{4+} + e^- \longrightarrow Ti^{3+}$$

$$O^{2-} + 2h^+ \longrightarrow 1/2O$$

Figure S2. Schematic diagram of the mechanism that the oxygen vacancy-Ti^{3+} generation process (Xiong et al., 2012; Bennett et al., 2015; Yu et al., 2011; Zhang et al.2013), related to Figure 2.
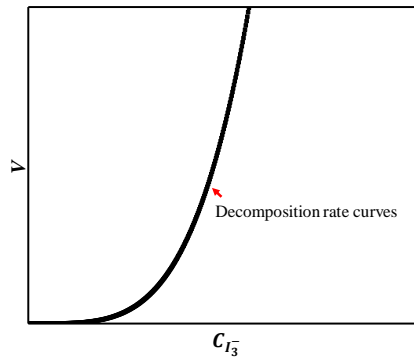
The graph shows axes labeled V (vertical) and $C_{I_3^-}$ (horizontal) with a curve annotated "Decomposition rate curves"

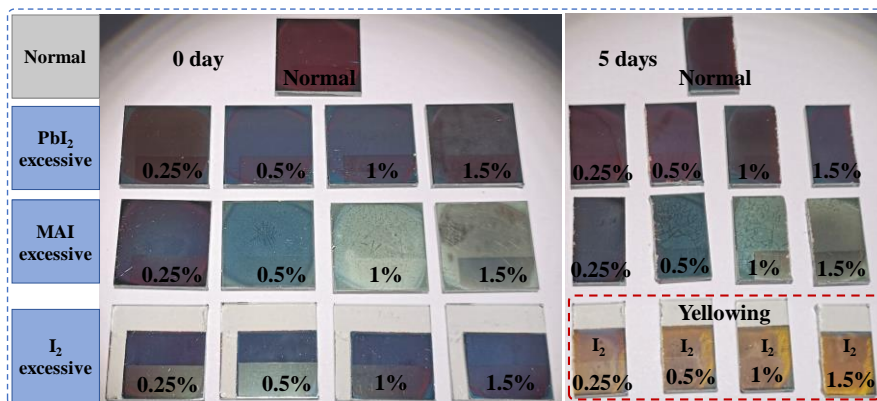**Figure S3. The curve corresponding the formula of perovskite decomposition rate, related to Figure 2.**

Figure S4. Perovskite film with different doping ratios of PbI$_2$, MAI and I$_2$ for different UV exposure time (0 day and 5days), related to Figure 2.
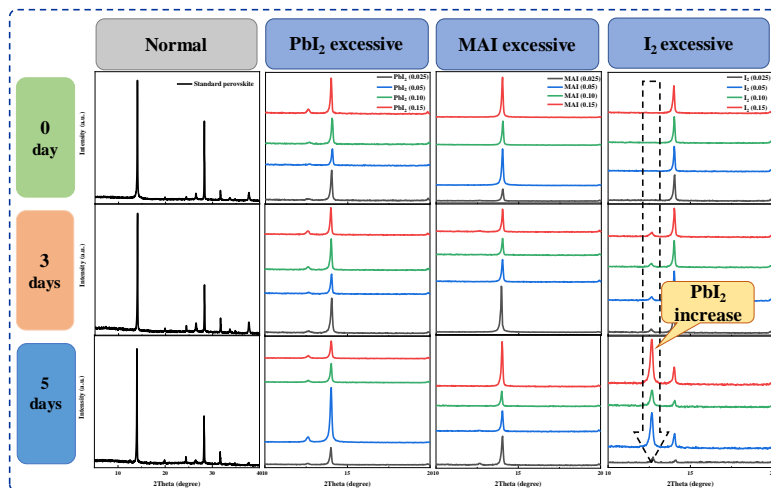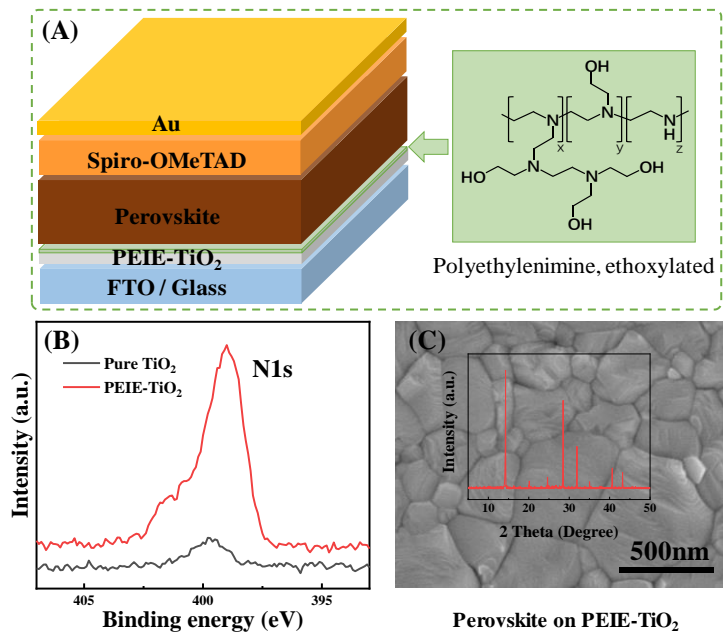

Figure S5. XRD patterns of perovskite film with different doping ratios of PbI$_2$, MAI and I$_2$ for different UV exposure time (0 day, 3 days and 5 days), related to Figure 2.

Figure S6. Structure and crystallinity of the perovskite solar cell, related to Figure 2.

(A) Schematic of the device structure and the molecular structure of PEIE.

(B) Top-view SEM images of perovskite films on PEIE-TiO$_2$ ETL, and the inserted image is the XRD patterns of the corresponding perovskite film.

(C) XPS pattern of N1s core level on the pure TiO$_2$ and PEIE-TiO$_2$ substrate.
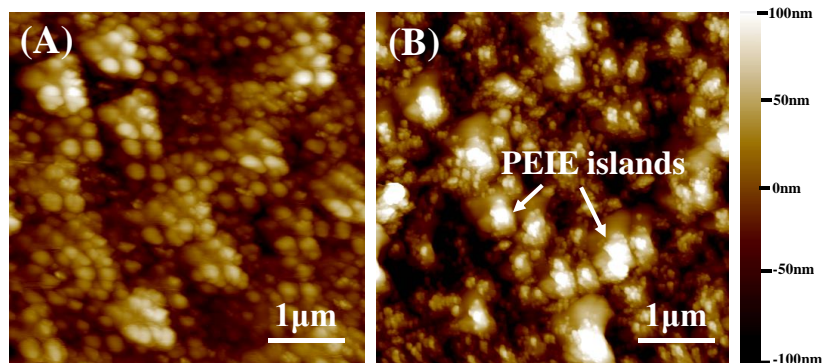
Figure S7. The AFM image of TiO$_2$ ETL surface morphology, related to Figure 3.

(A) The pure TiO$_2$ ETL.
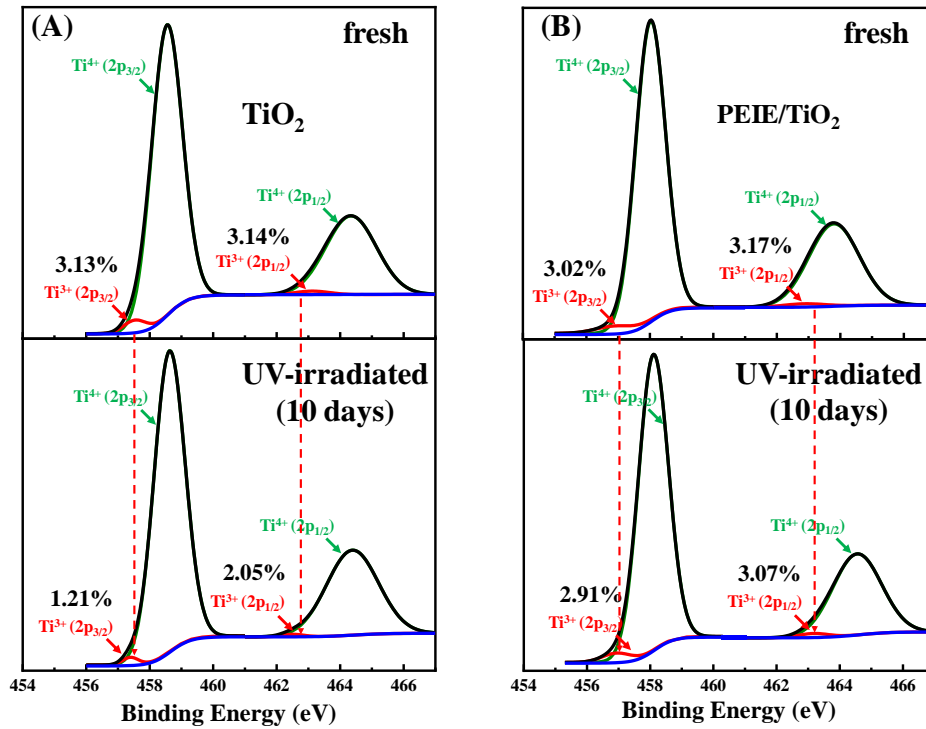
(B) The PEIE-modified TiO$_2$ ETL.

Figure S8. XPS Ti(2p) spectra of (A) pure-TiO₂ film and (B) PEIE-TiO₂ film on glass under UV irradiation for 0 day and 10 days, related to Figure 3.
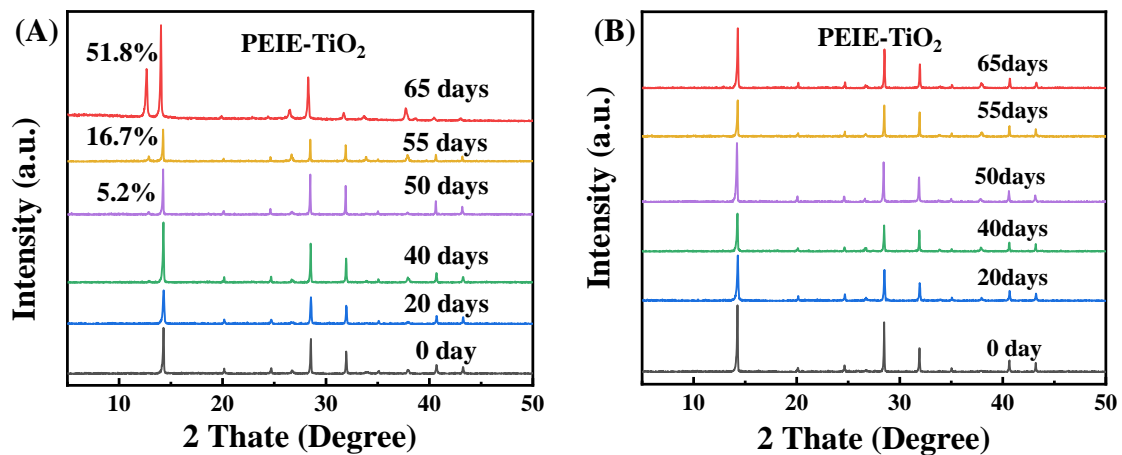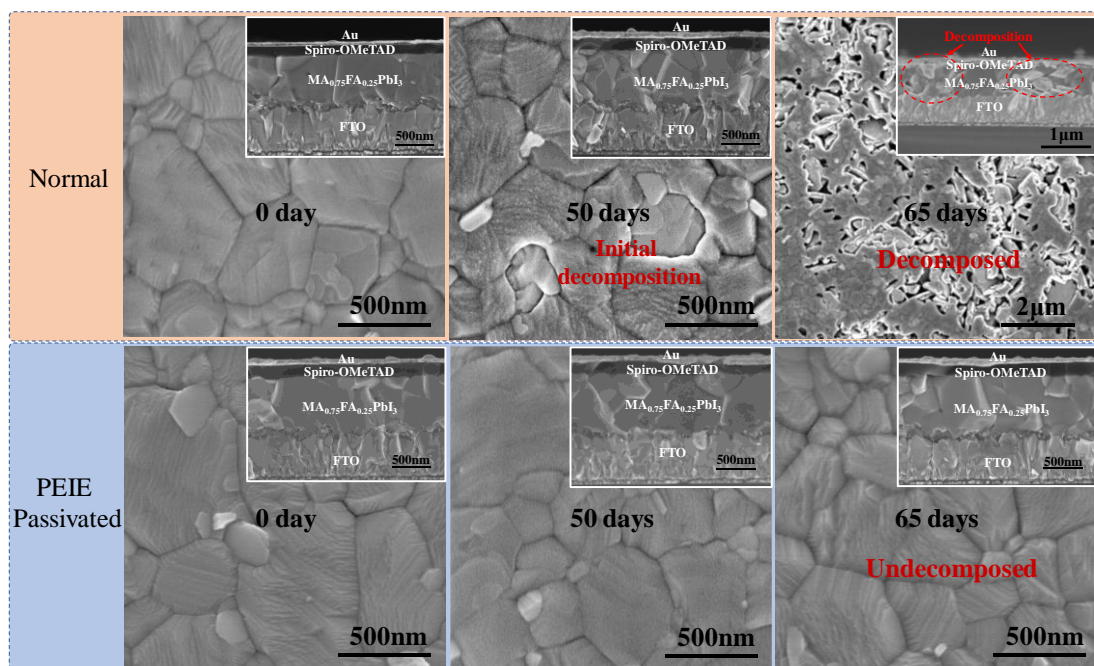

Figure S9. XRD patterns of perovskite film in PSCs based on (A) pure-TiO₂ ETL and (B) PEIE-TiO₂ ETL under UV irradiation, related to Figure 4.

Figure S10. Morphology evolution of perovskite films under UV exposure, related to Figure 4. The scanning electron microscope (SEM) images of the perovskite films deposited on pure-TiO$_2$ ETL (top) and PEIE-TiO$_2$ (bottom) after UV irradiation for 0, 50, 65 days.
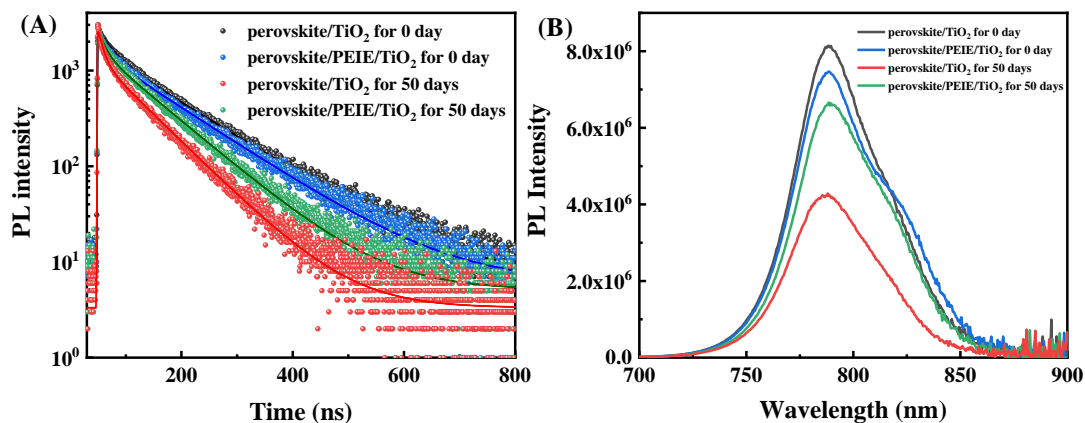
Figure S11. Photoluminescence spectrum of perovskite film on pure TiO$_2$ ETL and PEIE-modified TiO$_2$ ETL under UV irradiation for 0 day and 50 days in glovebox. Related to Figure 5.

(A) Steady photoluminescence (PL) spectrum of perovskite film.

(B) Transient photoluminescence (TRPL) decay of perovskite film.

The inset table in the figure:

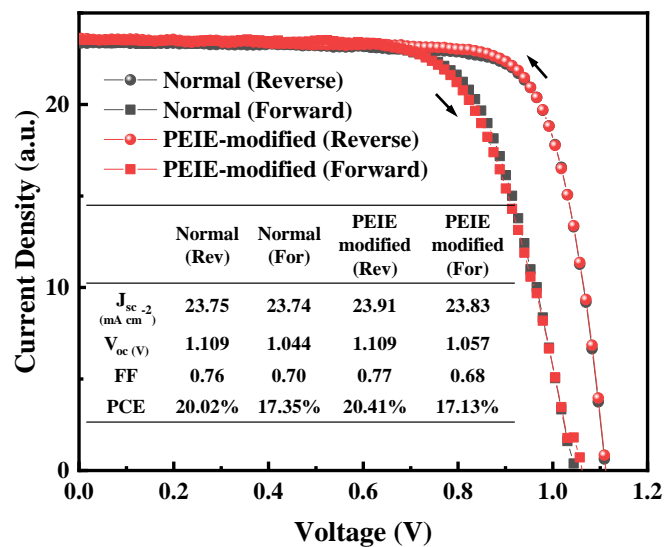|	Normal (Rev)	Normal (For)	PEIE modified (Rev)	PEIE modified (For)
J_{sc} (mA cm^{-2})	23.75	23.74	23.91	23.83
V_{oc} (V)	1.109	1.044	1.109	1.057
FF	0.76	0.70	0.77	0.68
PCE	20.02%	17.35%	20.41%	17.13%

Figure S12. Forward (roundness) and reverse (square) scanned J-V curves of the PSCs with (red) and without (black) PEIE layer. Inset: Device performance parameters calculated from the curves. Related to Figure 5.

Table S1. The fitting values of R_t and R_{rec} based on the EIS Nyquist plots, related to Figure 4.

	R_t (kΩ)	R_{rec} (kΩ)
Pure TiO$_2$ for 0 day	64.296	58.330
PEIE/TiO$_2$ for 0 day	61.370	76.690
Pure TiO$_2$ for 6 days	89.330	48.230
PEIE/TiO$_2$ for 6 days	65.748	69.330

Transparent Methods

Materials:

Methylammonium iodide, formamidinium iodide, 2,2',7,7'-tetrakis (N, N-di-p-methoxyphenylamine)-9,9' spirobifluorene (spiro-OMeTAD) and Li-bis(trifluoromethanesulfonyl) imide (Li-TFSI) were purchased from Xi'an Polymer Light Technology Corp. (Purity: 99.5%). Lead iodide (Purity:99.999%), FK209, titanium tetrachloride ($TiCl_4$, Purity:99.9%) precursor were purchased from Alfa Aesar. N, N-Dimethylformamide (DMF), dimethyl sulfoxide (DMSO), and chlorobenzene were purchased from Acros Organics (Extra dry). Polyethylenimine, 80% ethoxylated (PEIE) was dissolved in H_2O with a concentration of 37 wt. % in H_2O when received from Aldrich.

Device Fabrication：

Solution Preparation: TiO_2 solution was prepared according to the report of Wei et al (Dei et al., 2017). 1 mL of $TiCl_4$ precursor was dropwise added into 50 mL of ultrapure water, and stir it up. To prepare the perovskite precursor solution, 0.25 M of FAI, 0.75 M of MAI, and 1.025 M of PbI_2 were mixed in anhydrous dimethylformamide/dimethylsulfoxide (600 mg/78 mg) solution, which was stirred for 2 h at room temperature in the glove box. To prepare the HTM precursor, Spiro-OMeTAD was solved in chlorobenzene with the concentration of 80 mg·mL^{-1} and then tert-butylpyridine (28.5 μL in 1 mL chlorobenzene), and lithium bis-(trifluoromethanesulfonyl) imide (8.75 mg·mL^{-1}) were added into the Spiro-OMeTAD solution as the additives, which was stirred in the glove box for 6 h as previous works (Song et al., 2016; Cui et al., 2017). To prepare the PEIE precursor solution, it was further diluted with 2-methoxyethanol (hereafter referred to as methoxyethanol) to a weight concentration of 0.1%.

Perovskite Solar Cell Fabrication: FTO glass (7 Ω·sq^{-1}) was cleaned by sequential sonication with a detergent solution, deionized water, acetone, and isopropyl alcohol for 20 min, respectively. After dried by a nitrogen flow, the substrates were treated with UV-ozone for 15 min before use. TiO_2 films were fabricated by water-bath heating the precursor solution onto the FTO substrates at 70℃ for 30 min. The, TiO_2 films were further treated with UV-ozone for 15 min and then transferred into the N_2-filled glove box. To fabricate perovskite films, the perovskite precursor was spin coated directly on the TiO_2 substrate at 4000 rpm for 30 s. During the spin-coating step, 0.5 mL diethyl ether was poured on the surface at 22 s before the end. The light-yellow transparent films were converted into the brownish-red perovskite films by heating at 110 °C for 15 min. Then the Spiro-OMeTAD solution was spin-coated at 4000 rpm for 30 s on the perovskite films. Finally, 80 nm Au electrode was evaporated on the films. For the PEIE-modified PSCs, the diluted PEIE solution was spin coated on top of the compact TiO_2 layer at a speed of 5000 rpm for 30 s. Spin-coated PEIE films were annealed at 100 ºC for 10 min on a hotplate in glovebox. Finally, the modified PSCs were fabricated according to the above method.

UV Aging and device monitored：

We used Philip UV lamp (λ = 254 nm) with an intensity of ~50 mW·cm^{-2} (equivalent to 11 suns of UV light below 400nm) to irradiate the PSCs from the TiO_2 ETL side at room temperature in an argon-filled glovebox. To achieve long-time efficiency monitoring, we designed and assembled an apparatus of stability test device. We attach the PSCs to the

platform of the apparatus so that it can be irradiated by UV light. Then, the apparatus containing the PSCs was transferred to the UV radiation chamber, which is installed in an argon-filled glovebox. The apparatus is sealed and removed every 24h to measure the current voltage curves under simulated AM 1.5G 100 mW·cm^{-2} irradiance.

Device Characterization：

Current-voltage curves were measured using a source meter (Keithley 2400) under AM 1.5G irradiation with a power density of 100 mW·cm^{-2} from a solar simulator (XES-301S+EL-100) by forward (-0.1 to 1.2 V) or reverse (1.2 to-0.1 V) scans. The light intensity was calibrated with a NIM-certified Si reference cell. The step voltage was fixed at 12 mV and the delay time was set at 10 ms. All PSCs were fabricated with a metal mask that was used to define the active area, which is 0.1 cm^2. XPS spectra were collected using a Thermo Fisher Scientific ESCALAB 250Xi under 10^{-9} Torr vacuum using a monochromic Al-Ka X-ray source. Fitting procedures to extract peak positions and relative element content from the XPS data were carried out using the Origin software. The UPS spectra were also measured by XPS (ESCSLAB 250Xi). All spectra were shifted to account for sample charging using inorganic Au as a reference. The steady PL spectra of the perovskite films on FTO substrates were measured by a spectrometer (Edinburg PLS 980) at 80 K. The EQE was measured using QE-R systems (Enli Tech.). The EIS patterns of the PSCs were measured by a electrochemical workstation (Zahner Zennium). The absorption spectrums were measured by UV-VIS spectrophotometer (UV-2600). The morphologies of the as-prepared MA$_{0.75}$FA$_{0.25}$PbI$_3$ were characterized by scanning electron microscopy (SEM) (FEI SIRION 200). The chemical compositions and structures of the MA$_{0.75}$FA$_{0.25}$PbI$_3$ films were analyzed by X-ray diffraction (XRD) (Bruker D8 Advance X-ray diffractometer, Cu-Kα radiation λ= 0.15406 nm).
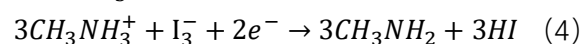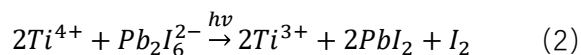
Formula derivation:

Reaction rate formula based on the mass action law:

$$v = kc_A^a c_B^b \qquad \text{Formula S1.}$$

The detail derivation process of the formula:

$$V = 8kx^4(1 + \frac{1}{Kc(I^-)})^3$$

The decomposition procedures of perovskite material in terms of chemical equations:

$$Ti^{3+} \xrightarrow{h\nu} Ti^{4+} + e^- \qquad\qquad (1)$$

$$2Ti^{4+} + Pb_2I_6^{2-} \xrightarrow{h\nu} 2Ti^{3+} + 2PbI_2 + I_2 \qquad (2)$$

$$I_2 + I^- = I_3^- \qquad\qquad\qquad\qquad (3)$$

$$3CH_3NH_3^+ + I_3^- + 2e^- \rightarrow 3CH_3NH_2 + 3HI \quad (4)$$

According to the mass action law, the reaction rate of Equation 4 can be calculated by

$$V = kc_{MA}^3 c_{I_3^-}^1$$

where V is the reaction rate, k is the chemical reaction rate constant, C_{MA} is the qualitative concentration of $CH_3NH_3^+$, $C_{I_3^-}$ is the qualitative concentration of I_3^-. Based on Equation 2, the C_{MA} can be written as: $C_{MA} = 2(C_{I_2} + C_{I_3^-})$.

Given that $x = c(I_3^-), y = c(I_2)$, the $v = k(2(x + y))^3 x$.

Then, $v = k (8(x^3+3x^2y+3xy^2+y^3) x$, $v=8k (x^4+3x^3 y+3x^2 y^2+xy^3)$.

For the Equation 3, when it is in equilibrium, $K = \frac{c(I_3^-)}{c(I_2)c(I^-)}$, where K is the chemical equilibrium constant. Hence, $K = \frac{x}{yc(I^-)}$, $y = \frac{x}{Kc(I^-)}$.

Therefore, $v = 8k \left(x^4 + 3x^3 \frac{x}{Kc(I^-)} + 3x^2 \frac{x^2}{K^2c(I^-)^2} + x \frac{x^3}{K^3c(I^-)^3}\right)$.

Finally, $v = 8kx^4(1 + \frac{1}{Kc(I^-)})^3$.

Supplemental References

Xiong, L.-B.; Li, J.-L.; Yang, B.; Yu, Y. J. (2012). Ti^{3+} in the surface of titanium dioxide: generation, properties and photocatalytic application. Nanomater. *2012*, 9.

Bennett, T.; Adnan, R. H.; Alvino, J. F.; Kler, R.; Golovko, V. B.; Metha, G. F.; Andersson, G. G. (2015). Effect of Gold Nanoclusters on the Production of Ti^{3+} Defect Sites in Titanium Dioxide Nanoparticles under Ultraviolet and Soft X-ray Radiation. J. Phys. Chem. C *119*, 11171-11177.

Yu, Y.; Wu, K.; Wang, D. (2011). Dye-sensitized solar cells with modified TiO_2 surface chemical states: The role of Ti^{3+}. Appl. Phys. Lett. *99*, 192104.

Zhang, X.; Tian, H.; Wang, X.; Xue, G.; Tian, Z.; Zhang, J.; Yuan, S.; Yu, T.; Zou, Z. (2013). The role of oxygen vacancy-Ti^{3+} states on TiO_2 nanotubes' surface in dye-sensitized solar cells. Mater. Lett. *100*, 51-53.

Dei, D.; Ji, J.; Song, D.; Li, M.; Cui, P.; Li, Y.; Mbnegue, J. M.; Zhou, W.; Ning, Z.; Park, N. G. (2017). A TiO_2 embedded structure for perovskite solar cells with anomalous grain growth and effective electron extraction. J. Mater. Chem. A *5*, 1406-1414.

Song, D.; Wei, D.; Cui, P.; Li, M.; Duan, Z.; Wang, T.; Ji, J.; Li, Y.; Mbengue, J. M.; Li, Y.; He, Y.; Trevora, M.; Park, N. G. (2016). Dual function interfacial layer for highly efficient and stable lead halide perovskite solar cells. J. Mater. Chem. A *4*, 6091-6097.

Cui, P.; Wei, D.; Ji, J.; Song, D.; Li, Y.; Liu, X.; Huang, J.; Wang, T.; You, J.; Li, M. (2017). Highly Efficient Electron-Selective Layer Free Perovskite Solar Cells by Constructing Effective p-n Heterojunction. Solar Rrl *1*, 1600027.